

# Footprints of Atlantic Multidecadal Oscillation in the Low-Frequency Variation of Extreme High Temperature in the Northern Hemisphere

MIAONI GAO

*Beijing Normal University, Beijing, China*

JING YANG, DAOYI GONG, AND PEIJUN SHI

*Key Laboratory of Environmental Change and Natural Disaster, Ministry of Education, and State Key Laboratory of Earth Surface Processes and Resource Ecology, Faculty of Geographical Science, Beijing Normal University, Beijing, China*

ZHANGANG HAN

*School of Systems Science, Beijing Normal University, Beijing, China*

SEONG-JOONG KIM

*Division of Polar Climate Sciences, Korea Polar Research Institute, Incheon, South Korea*

(Manuscript received 12 July 2018, in final form 20 November 2018)

## ABSTRACT

The frequency and intensity of extreme high temperature (EHT) in the Northern Hemisphere exhibit remarkable low-frequency (LF) variations (longer than 10 years) in summer during 1951–2017. Five hotspots featuring large LF variations in EHT were identified, including western North America–Mexico, eastern Siberia, Europe, central Asia, and the Mongolian Plateau. The probability density functions show that the higher EHT occurrences over these hotspots in recent decades is consistent with the shifted average and increased variances in daily mean temperature. The common features of the LF variation in EHT frequency over all domains are the remarkable increasing trends and evident decadal to multidecadal variations. The component of decadal to multidecadal variations is the main contribution to the LF variations of temperature in the last century. Further analysis shows that the coherent variability of decadal to multidecadal temperature variations over western North America–Mexico, eastern Siberia, Europe, and the Mongolian Plateau are the footprints of a dominant natural internal signal: the Atlantic multidecadal oscillation. It contributes to the variations in temperature over these hotspots via barotropic circumglobal teleconnection, which imposes striking anomalous pressure over these regions. This study implies that natural internal variability plays an important role in making hotspots more vulnerable to EHT.

## 1. Introduction

Extreme high temperature (EHT) has widespread impacts on human health, society, economies, and ecosystems (Easterling et al. 2000; National Academies of Sciences, Engineering, and Medicine 2016). In recent years, severe EHT events have significantly increased

and hit various parts of the globe (Alexander et al. 2006)—for example, EHT occurred during the summer of 2010 in Russia (Grumm 2011), summer 2013 in eastern China (Wang et al. 2017), and summer 2015 in India (Dodla et al. 2017). Recognizing global hotspots of low-frequency (LF) variations in EHT and understanding the reasons for their features are crucial in the mitigation of risks and in adaptations to climate change (Eyring et al. 2016).

As a result of the limited availability of high-quality global observational datasets, previous studies have primarily investigated the LF variation

---

 Denotes content that is immediately available upon publication as open access.

---

Corresponding author: J. Yang, yangjing@bnu.edu.cn

DOI: 10.1175/JCLI-D-18-0446.1

© 2019 American Meteorological Society. For information regarding reuse of this content and general copyright information, consult the [AMS Copyright Policy](https://www.ametsoc.org/PUBSReuseLicenses) ([www.ametsoc.org/PUBSReuseLicenses](https://www.ametsoc.org/PUBSReuseLicenses)).

in temperature extremes from a spatially aggregated perspective or on a regional scale. Global-average EHT has been reported to show an increasing trend from 1951 to 2003 (e.g., Alexander et al. 2006; Fischer and Knutti 2014). Meanwhile, the characteristics of the LF variation in EHT in some regions such as Europe (Kysely 2009), China (Qi and Wang 2012), and North America (Grotjahn et al. 2016) have attracted the interest of researchers. However, whether these regions are more vulnerable to EHT than others is unclear.

The characteristics of the LF variation in EHT differ from region to region. Generally speaking, EHT over most global land areas have shown increasing trends of varying degrees (e.g., Grotjahn et al. 2016; Rohini et al. 2016; Wibig 2018). But the severities of EHT in different domains are not comparable, because they have been derived from different datasets using different criteria. In addition, EHT in some areas shows a remarkable decadal to multidecadal variation. For instance, the warm days over the Mongolian Plateau shows prominent changes around the 1980s and 1990s (Wang et al. 2016). Europe experienced anomalously strong EHT during the time periods 1936–49 and 1992–2005 (Della-Marta et al. 2007). However, whether there is a link between the LF variations in EHT in these regions remains unknown.

Previous studies have reported that the long-term trends in EHT can be mainly ascribed to anthropogenic forcing (Stott et al. 2004; Sun et al. 2014). However, the contribution of natural forcing to the decadal to multidecadal variation in temperatures and EHT varies widely in different regions. For instance, the Atlantic multidecadal oscillation (AMO) and natural external forcing (solar forcing, volcanic eruptions, and sulfate aerosols) could influence the summer temperature/EHT over Europe (Boer et al. 2000; Ghosh et al. 2017). Ruprich-Robert et al. (2018) suggested that the soil moisture content contributes to heat waves over North America. The decadal variation in the frequency of EHT over Eurasia has been reported to be influenced by mega-El Niño–Southern Oscillation and AMO (Zhou and Wu 2016). These diversities motivated us to investigate the dominant natural contributors for each core region and their linkages. As two of the most important natural internal variabilities on the decadal to multidecadal time scales that could influence the climate in local and remote regions (e.g., Sutton and Hodson 2005; Sun et al. 2015; Dong and Dai 2015), AMO and interdecadal Pacific oscillation (IPO) become a major focus.

Based on several indices of global temperature extremes constructed from global in situ observations

(Donat et al. 2013), we addressed three questions: 1) what are the LF hotspots of summertime EHT in the Northern Hemisphere, 2) is there coherent LF variation in EHT over these hotspots, and 3) if so, what controls the coherent variation in EHT in the hotspots? The remainder of this paper is organized as follows. Section 2 introduces the datasets and methods used in the study. The hotspots with a large LF variability of summer EHT in the Northern Hemisphere are identified in section 3, and the detailed characteristics of the LF variation in EHT over hotspots are presented in section 4. Section 5 identifies the footprints of the AMO on EHT over hotspots and proposes physical mechanisms for the connections. A discussion and summary are presented in sections 6 and 7, respectively.

## 2. Datasets and methodology

### a. Datasets

Extreme temperature indices were retrieved from the Gridded Temperature and Precipitation Climate Extreme Indices (GHCNDEX) dataset. This dataset was developed from the National Climatic Data Center's Global Historical Climatology Network-Daily dataset, which is the world's largest repository of daily in situ observations. It provides the 26 temperature and precipitation indices recommended by the World Meteorological Organization Commission for Climatology/CLIVAR/JCOMM Expert Team on Climate Change. Two variables, the monthly warm days and the warmest daily maximum temperature  $T_{\max}$ , were used in this study. The warm days refer to the EHT frequency, which are defined as the percentage of days with the daily maximum temperature exceeding the local 90th percentile of the base period 1961–90. The 90th percentile was calculated for each calendar day using a centered 5-day window. The spatial resolution is  $2.5^\circ$ , and the record covers the time period 1951–2017 (Donat et al. 2013). The results were verified by the daily maximum and mean temperatures from the Berkeley Earth Surface Temperatures (BEST) dataset provided by the Berkeley Earth Project (Levi 2013; Rohde et al. 2013a,b). The BEST data have a horizontal resolution of  $1^\circ$  and cover the time period 1920–2017. As the stations in the GHCNDEX dataset are mainly distributed in the Northern Hemisphere, this study focused on boreal summer [June–August (JJA)] EHT in the Northern Hemisphere.

The other monthly temperature variables used in this study include the monthly surface air temperature

from the GISS Surface Temperature Analysis (GISTEMP) dataset with a horizontal resolution of  $2^\circ$  over the time period 1920–2017 (Hansen et al. 2010) and the National Oceanic and Atmospheric Administration (NOAA) Extended Reconstructed Sea Surface Temperature, version 5 (ERSST.v5) with a horizontal resolution of  $2^\circ$  over the time period 1920–2014 (Huang et al. 2015; Liu et al. 2015).

The monthly mean atmospheric circulation, radiative flux, and cloud cover were provided by 1) the National Centers for Environmental Prediction–National Center for the Atmospheric Research (NCEP–NCAR) reanalysis datasets with a spatial resolution of  $2.5^\circ$  and 17 pressure levels in the vertical direction over the time period 1951–2017 (Kalnay et al. 1996), 2) the Twentieth Century Reanalysis, version 2 (20CR), data products with a spatial resolution of  $2^\circ$  and 24 pressure levels (Compo et al. 2011) from the NOAA over the time period 1920–2014, and 3) the European Centre for Medium-Range Weather Forecasts (ECMWF) twentieth century reanalysis (ERA-20C) dataset with a spatial resolution of  $2.58^\circ$  and 37 pressure levels over the time period 1920–2010 (Poli et al. 2016). Data records after 1920 were used because the observations of sea surface temperature (SST) are sparse over the tropical Pacific before the 1920s (Dong and Dai 2015). Note that the surface variables in 20CR only cover the time period 1920–2012. The AMO and IPO indices were downloaded from the NOAA website (Enfield et al. 2001; Henley et al. 2015).

### b. Methodology

In this study, we focused on the LF variations in EHT and temperature. The Theil–Sen trend estimation method and the Mann–Kendall trend significance test were used to extract linear trends (Mondal et al. 2012). The LF variation of any field of interest was extracted by filtering out interannual variations shorter than 10 years via the Lanczos filter (Duchon 1979), which only allows components with time periods longer than 10 years. Thus, it contains the decadal to multidecadal variabilities and long-term trends of the time series. The decadal to multidecadal variations of hotspot-averaged EHT and temperature were calculated by simply removing the linear trends of time series. To better remove the larger-scale global signal associated with global warming, the decadal to multidecadal variations of other variables of interest were obtained by removing the signals associated with the LF variations of the globally averaged SST from them using linear regression analysis. We fitted the globally averaged SST to the LF variables using the least squares technique. The estimated components related to the SST

were then subtracted from the climate time series and the residuals were regarded as the parts that were dominated by decadal to multidecadal variations (Wu et al. 2016). The data were averaged using the cosine of the latitude as the weight. The statistical significance was evaluated using the Student's *t* test with autocorrelation to estimate the effective degree of freedom (Zwiers and von Storch 1995).

According to Yanai et al. (1973), the change in temperature at each constant level is determined by the combined effects of the horizontal temperature advection ( $-\mathbf{V} \cdot \nabla T$ ), the adiabatic process  $\omega\sigma$  related to vertical motion and the atmospheric apparent heat source  $Q_1$ , where  $T$  denotes the temperature,  $\mathbf{V}$  is the horizontal velocity vector,  $\nabla$  is the horizontal gradient operator,  $\omega$  is the vertical pressure velocity,  $\sigma = RT/(c_p p) - \partial T/\partial p$  is the static stability,  $p$  is the pressure,  $c_p$  denotes the specific heat at constant pressure, and  $R$  is the gas constant. Because  $Q_1$  is largely modulated by the net upward flux at the boundary layer, the horizontal temperature advection, the adiabatic process, and the surface radiative fluxes were analyzed to understand the heating process.

### 3. Hotspots of EHT with LF variations

To identify the hotspots of LF changes in EHT, we showed the spatial distribution of LF changes in EHT by calculating the contribution of the LF variance against the total variance in EHT for both the EHT frequency (warm days) and intensity (warmest  $T_{\max}$ ) during the boreal summers of 1951–2017 in the Northern Hemisphere (Fig. 1).

Here, we defined an EHT hotspot as a region in which the fractional LF variance of both the frequency and intensity exceed the top tertile of the values in the Northern Hemisphere. The top tertile thresholds of the fractional variance are 28.7% and 26.9% for the frequency and intensity, respectively. In this way, five hotspots of EHT were identified: western North America–Mexico ( $15^\circ$ – $42^\circ$ N,  $115^\circ$ – $98^\circ$ W), eastern Siberia ( $52^\circ$ – $71^\circ$ N,  $128^\circ$ E– $180^\circ$ ), Europe ( $37^\circ$ – $55^\circ$ N,  $4^\circ$ W– $46^\circ$ E), central Asia ( $31^\circ$ – $53^\circ$ N,  $52^\circ$ – $78^\circ$ E), and the Mongolian Plateau ( $41^\circ$ – $60^\circ$ N,  $88^\circ$ – $122^\circ$ E). These regions were considered to be more vulnerable to EHT as a result of their large LF fluctuations.

### 4. Characteristics of the LF change in EHT and the daily mean temperature over hotspots

What are the major features of LF change in EHT over the above hotspots? To address this question, we used the warm days to represent EHT because warm

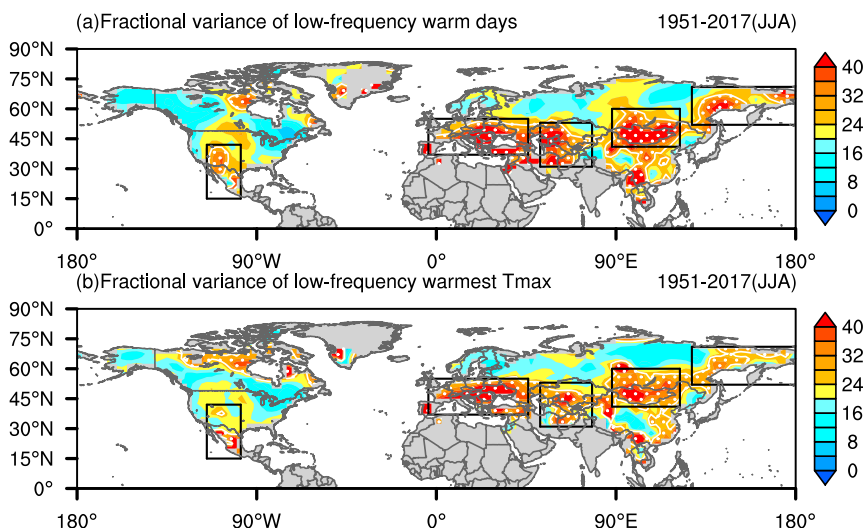


FIG. 1. The fractional variance of LF (a) warm days (%) and (b) warmest daily  $T_{\max}$  (%) in JJA during the time period 1951–2017. The five black boxes denote the hotspots of western North America–Mexico, eastern Siberia, Europe, central Asia, and the Mongolian Plateau. The white dots and lines denote the areas with values exceeding top tertile of the grids in the Northern Hemisphere.

days had fewer missing values than the data of the warmest  $T_{\max}$  in the GHCNDEX dataset. Because the more recent decades from the early 1980s are likely to be the warmest 30-yr period of the last 1400 years in the Northern Hemisphere (IPCC 2014), we purposely separated the 67 summers into two periods: 1951–79 and 1980–2017. By comparing the two epochal differences in the occurrence of EHT over the hotspots (Fig. 2a), we found that the probability density functions (PDFs) of warm days in the post-1980 epoch shift remarkably toward larger values, indicating that the occurrences of EHT significantly increase. The maximum PDF value of the EHT frequency averaged over the five hotspots increases by 2.53% after 1980. We also found that the daily mean temperatures shift to the warmer side, which is consistent with the changes in the occurrence of EHT. The maximum PDF value of the daily mean temperature averaged over the hotspots increases by 0.48°C after 1980. In addition, the distribution of the PDF of daily mean temperatures become flatter in all the hotspots, indicating the increased variability of temperature after the 1980s. Both the shifted average and the increased variability in the daily mean temperature lead to the occurrence of more EHT over the five hotspots.

By examining the annual time series of the region-averaged frequency of EHT in each hotspot from 1951 to 2017, we found that the shift around the 1980s contains changes on two different time scales: a long-term trend and decadal to multidecadal variations (Fig. 3).

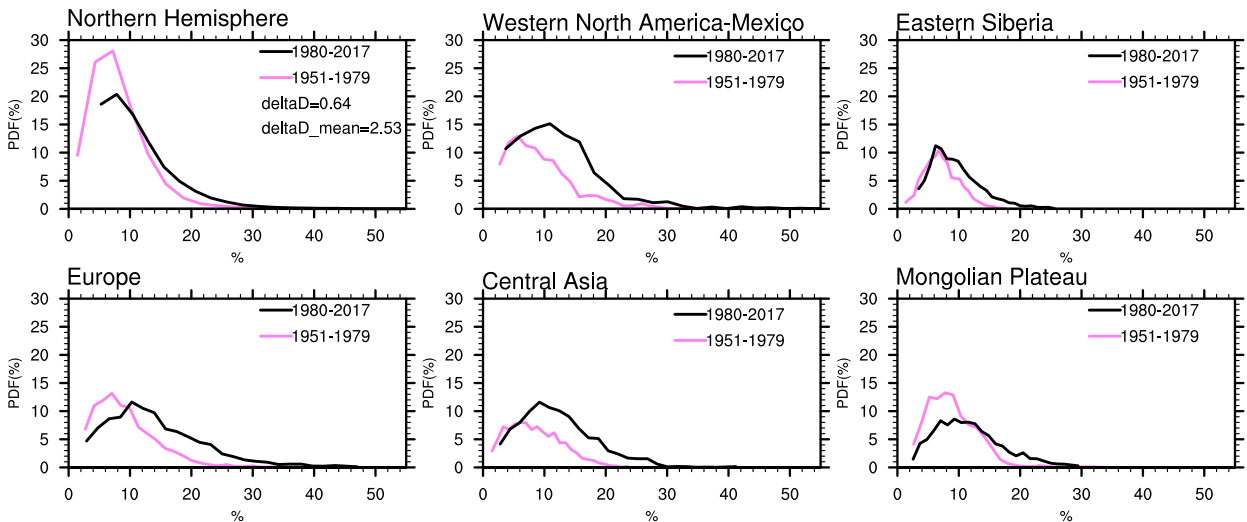
The linear trends in the EHT frequencies are significantly positive over all hotspots, with values of 0.82%–1.95% decade<sup>-1</sup> over the five hotspots and an average of 1.29% decade<sup>-1</sup>. The large decadal to multidecadal variation is also significant over each hotspot, accounting for 22.9%–47.7% of the total LF variance. According to the Lepage changepoint test (Lepage 1971), the decadal changes in the EHT over most hotspots mainly occur around the early 1960s and mid-1990s (table not shown).

Is there any linkage between EHT and associated daily mean temperature in their LF change? The correlation coefficients of the decadal to multidecadal variations in EHT and the mean temperature over the five hotspots range from 0.73 to 0.97, which are all significant at 99% confidence level (Fig. 4). Therefore, both the PDF and the correlation analysis indicate that the LF changes in EHT are consistent with that of the daily mean temperature in the hotspots.

### 5. Coherency of the LF variations in EHT over hotspots

As mentioned above, the decadal to multidecadal variations in EHT account for 22.9%–47.7% of the total LF variance over the five hotspots during the time period 1951–2017. We further calculated the fractional variance of the decadal to multidecadal variations during 1920–2017 using the daily mean temperature and found that it explains 80.2%, 58.6%, 79.8%, 54%,

(a) Warm days



(b) Surface air T

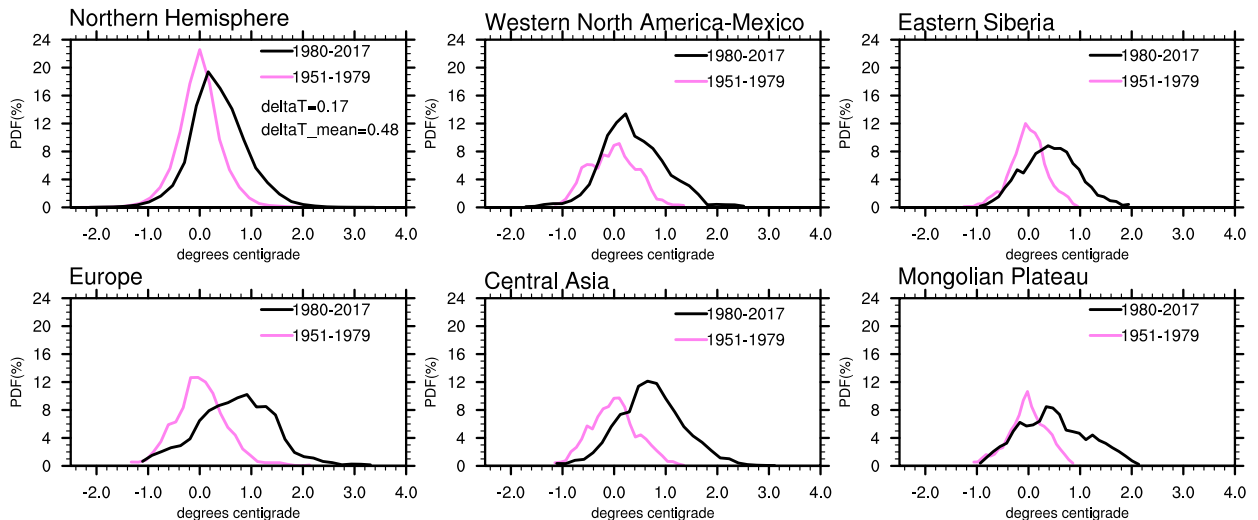


FIG. 2. PDF of (a) warm days (%) and (b) the surface air temperature anomaly (°C) in the Northern Hemisphere and over the five hotspots (western North America–Mexico, eastern Siberia, Europe, central Asia, and the Mongolian Plateau) during the time periods 1951–79 (pink) and 1980–2017 (black);  $\Delta D/\Delta T$  and  $\Delta D_{\text{mean}}/\Delta T_{\text{mean}}$  show the differences of the maximum values of PDFs between the periods of 1951–79 and 1980–2017 in the Northern Hemisphere and averaged over five hotspots, respectively.

and 98% of the LF variance averaged over western North America–Mexico, eastern Siberia, Europe, central Asia, and the Mongolian Plateau, respectively. In other words, the decadal to multidecadal variations make the primary contribution to the large LF variance in the last century. We therefore investigated whether there is a coherent variation in the decadal to multidecadal fluctuations over these hotspots.

We investigated whether the decadal to multidecadal fluctuations of EHT over the five hotspots are correlated with one another using pairwise correlation

analysis. Table 1 shows that there are high correlations among four hotspots: western North America–Mexico, eastern Siberia, Europe, and the Mongolian Plateau. The correlation coefficients range from 0.23 to 0.64 and most of them are statistically significant at the 95% confidence level. These results suggest that the decadal to multidecadal variations in EHT over the four hotspots exhibit a coherent variation.

Why do the EHT over these hotspots have coherent variations? It is commonly assumed that the decadal to multidecadal variations in EHT over these regions

## Warm days

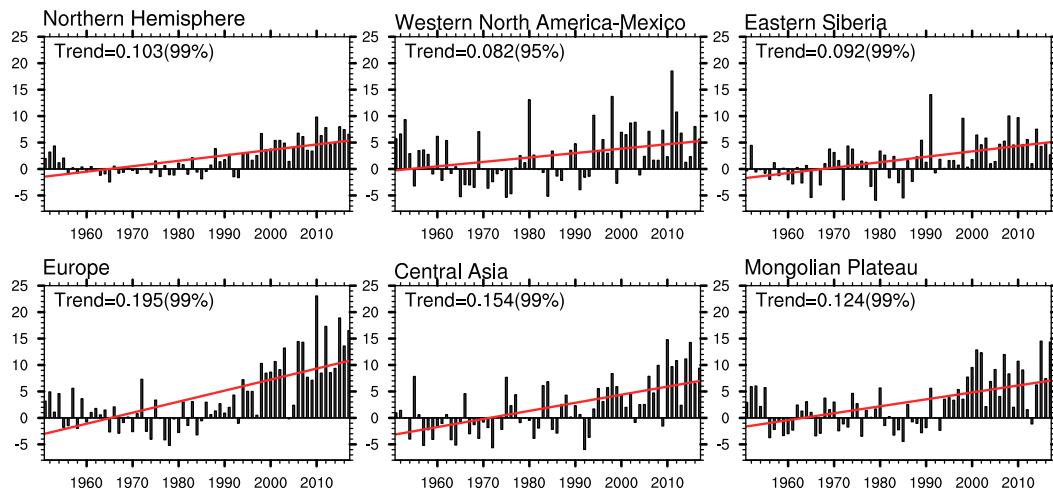


FIG. 3. Annual time series anomalies relative to the 1961–90 mean values for warm days (black bars; %) averaged over the Northern Hemisphere and the five hotspots (western North America–Mexico, eastern Siberia, Europe, central Asia, and the Mongolian Plateau) in the time period 1951–2017. The red lines are the linear regression lines and the values indicate linear trends in the Northern Hemisphere and at each hotspot ( $\% \text{ yr}^{-1}$ ).

are dominated by the same contributor. As the AMO and IPO are the most remarkable natural internal variabilities in decadal to multidecadal signals (e.g., McCabe et al. 2004; Sun et al. 2017), the relationship between the decadal to multidecadal variations in EHT and the AMO/IPO was examined (Table 2). We calculated the correlation coefficients between the AMO/IPO and the daily mean temperature over these hotspots derived from GISTEMP dataset rather than

EHT for two reasons. First, there is a consistent decadal to multidecadal variation between EHT and the daily mean temperature from 1951 to 2017 (section 4). Second, the records of the daily mean temperature (1920–2017) are longer than one life cycle of the AMO/IPO. Figure 4 shows that the temperature over western North America–Mexico, eastern Siberia, Europe, and the Mongolian Plateau are highly correlated with the AMO. In other words, during the positive

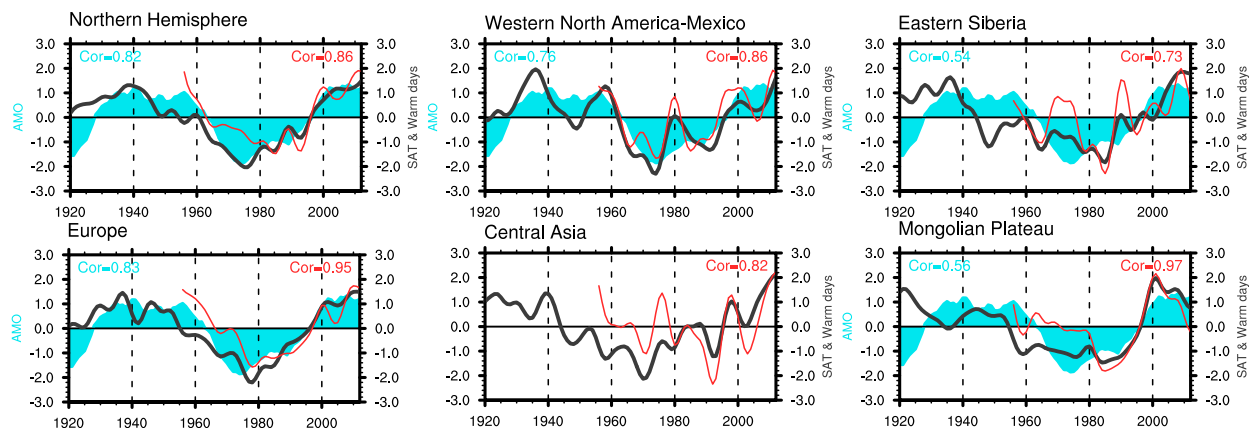


FIG. 4. Time series of the AMO (light blue shading) and decadal to multidecadal components of the surface air temperature (black line) and warm days (red line) in the Northern Hemisphere and five hotspots (western North America–Mexico, eastern Siberia, Europe, central Asia, and the Mongolian Plateau) during the time period 1920–2017. The blue values are the correlation coefficients between the AMO and surface air temperature during the time period 1920–2017 that are significant at the 99% confidence level. The red values are the correlation coefficients between the surface air temperature and EHT during the time period 1951–2017 that are significant at the 99% confidence level.

TABLE 1. Pairwise correlation coefficients of the decadal to multidecadal variations in EHT over the five hotspots during the time period 1951–2017. The boldface values indicate results significant at 95% confidence level.

Correlation coefficients (EHT)	Western North America–Mexico	Eastern Siberia	Europe	Central Asia	Mongolian Plateau
Western North America–Mexico	—	0.23	<b>0.64</b>	0.40	<b>0.52</b>
Eastern Siberia	0.23	—	<b>0.53</b>	0.11	<b>0.40</b>
Europe	<b>0.64</b>	<b>0.53</b>	—	0.49	<b>0.64</b>
Central Asia	0.40	0.11	0.49	—	0.29
Mongolian Plateau	<b>0.52</b>	<b>0.40</b>	<b>0.64</b>	0.29	—

(negative) phase of the AMO, anomalous warming (cooling) temperature and a greater (smaller) number of EHT days occur in these hotspots. The AMO explains 57.6% of the total variance in the decadal to multidecadal variations in temperature averaged over the five hotspots.

To understand how the AMO causes the decadal to multidecadal variations in temperature over these hotspots, the related temperature, atmospheric circulation, and radiative fluxes from GISTEMP and 20CR datasets were investigated (Figs. 5–7). Associated with AMO, a barotropic wave train in mid- to high latitudes, consisting of successive pressure troughs and ridges propagates from the North Atlantic to North America (Fig. 5). The most prominent feature of this wave train is the five salient maximum centers located over the North Atlantic Ocean, eastern Europe–Mediterranean Sea, the central Siberian Plateau–Mongolian Plateau, the western North Pacific, and the eastern North Pacific–western North America, which has also been found previously (Ding and Wang 2005; Wu et al. 2016; Si and Ding 2016). The integrated geopotential height anomalies in the troposphere show that these five maximum centers tend to have a larger intensity than other land areas (Fig. 5d). During the positive phase of the AMO, five high-pressure anomalies correspond to the location of four hotspots (western North America–Mexico, Europe, the Mongolian Plateau, and eastern Siberia).

Further temperature budget analysis (Yanai et al. 1973) was used to investigate the warming process over these hotspots associated with the circulation anomalies of the positive AMO (Fig. 6). The horizontal temperature advection and adiabatic heating at 850, 925, 925, and 850 hPa over western North America–Mexico, Europe, eastern Siberia, and the Mongolian Plateau were calculated because the mean surface pressures are 881, 969, 951, and 898 hPa in these regions, respectively. Although the temperatures are all associated with the anticyclones belonging to the AMO-related wave train, the heating processes over each hotspot differ from each other because the hotspots are influenced by different areas

of the anticyclones. The common feature over all the hotspots is that the increasing temperature should be ascribed to the combined effect of dynamical and diabatic heating processes. However, the near-surface warm horizontal temperature advection and adiabatic heating over Europe play the key role in heating the local temperature due to the significant wind anomalies and descending motion over this hotspot (Figs. 7a,b). In contrast, the warming over western North America–Mexico and eastern Siberia is dominated by diabatic heating, which is the enhanced upward longwave radiation fluxes and sensible heating caused by the reduced cloud cover and downward net solar radiation fluxes associated with the anticyclones (Fig. 6). Furthermore, both the significant warm temperature advection related to the anomalous southerlies at the west edge of the anticyclone and enhanced upward net longwave radiation caused by reduced cloud cover and downward net solar radiation contribute to the positive tendency over the Mongolian Plateau (Figs. 6, 7a).

## 6. Discussion

### a. Uncertainties in the impact factors for the variations in EHT over central Asia

The coherent variations in EHT over western North America–Mexico, eastern Siberia, Europe, and the Mongolian Plateau are considered to be the footprints of AMO. However, the mechanism for the decadal to

TABLE 2. Correlation coefficients of the AMO/IPO and decadal to multidecadal variations in temperature over the five hotspots in the GISTEMP and BEST datasets during the time period 1920–2017. The boldface values indicate results significant at 95% confidence level.

Correlation coefficients	AMO		IPO	
	GISTEMP	BEST	GISTEMP	BEST
Western North America–Mexico	<b>0.76</b>	0.06	<b>0.80</b>	–0.15
Eastern Siberia	<b>0.54</b>	0.01	<b>0.53</b>	–0.03
Europe	<b>0.83</b>	–0.18	<b>0.83</b>	–0.19
Central Asia	0.42	0.14	0.23	0.23
Mongolian Plateau	<b>0.56</b>	–0.25	<b>0.59</b>	–0.33

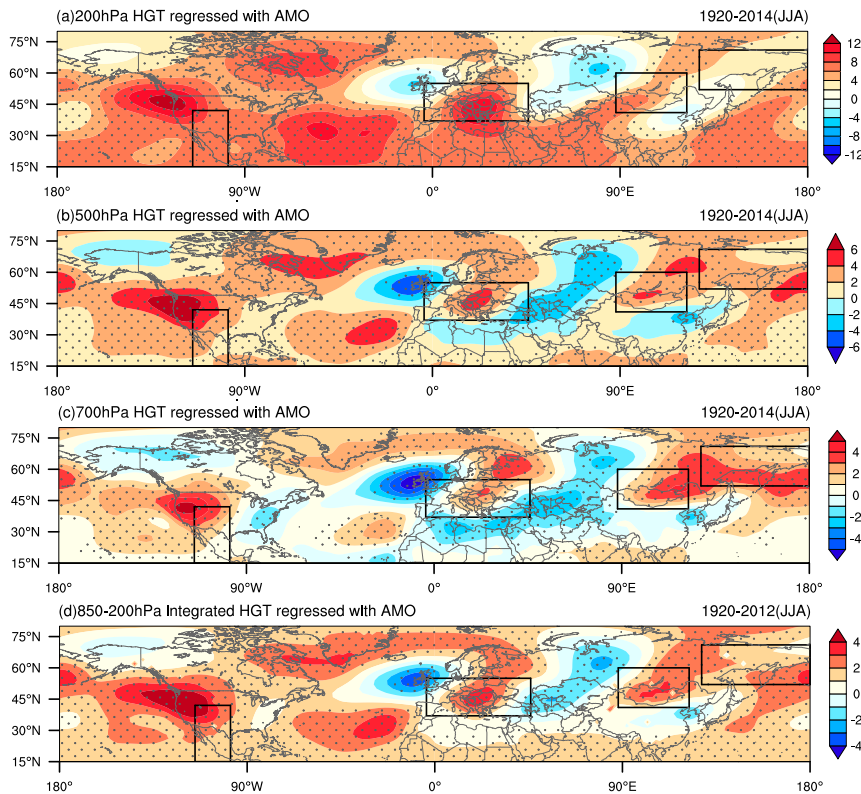


FIG. 5. The (a) 200-, (b) 500-, and (c) 700-hPa geopotential height anomalies (gpm) regressed to the AMO. (d) The 850–200-hPa integrated geopotential height anomalies ( $10^4$  gpm) regressed to the AMO. The dots show results significant at the 95% confidence level. The black boxes indicate the four hotspots of western North America–Mexico, eastern Siberia, Europe, and the Mongolian Plateau.

multidecadal variation of EHT over central Asia remains unclear. Although the temperature over this hotspot does not show a significant correlation with either the IPO or the AMO, the EHT and the temperature show considerable large decadal to multidecadal variability that accounts for 30.7% and 54% of the LF variation, respectively. Therefore, our hypothesis is that the EHT over central Asia might be influenced by the combined effect of the natural internal variability and natural external forcing. On the one hand, central Asia is influenced by a cyclonic anomaly belonging to the circumglobal teleconnection associated with the positive AMO, although the intensity is weaker than that at the five positive pressure centers (Fig. 5d). On the other hand, Watanabe and Yamazaki (2014a,b) have discussed the possible linkage between the heating over the northern Indian Ocean and the anticyclonic anomaly with increased temperature over central Asia on the decadal time scale. Accordingly, we calculated the correlation coefficient between the decadal to multidecadal components of SST averaged over the northern Indian Ocean ( $10^{\circ}\text{S}$ – $15^{\circ}\text{N}$ ,  $45^{\circ}$ – $110^{\circ}\text{E}$ ) and surface air

temperature over central Asia. The result shows that the coefficient is significant and indicates that the EHT over this hotspot might be affected by SST over the northern Indian Ocean. In addition, whether the EHT/temperature over central Asia could be influenced by other natural internal variability or external forcing still needs to be investigated in observation and numerical simulation.

#### *b. Comparison with other observational and reanalysis datasets*

To verify the robustness of our results, we compared them with global air temperatures and atmospheric circulations derived from other observational and reanalysis datasets. This study used the warm days and the daily mean temperature from the GHCNEX and GISTEMP datasets because both these datasets are based on GHCN-daily in situ observations and are therefore consistent with each other. To verify the results, we first identified the hotspots using daily global surface temperature anomalies from another dataset for comparison: the BEST dataset provided by the

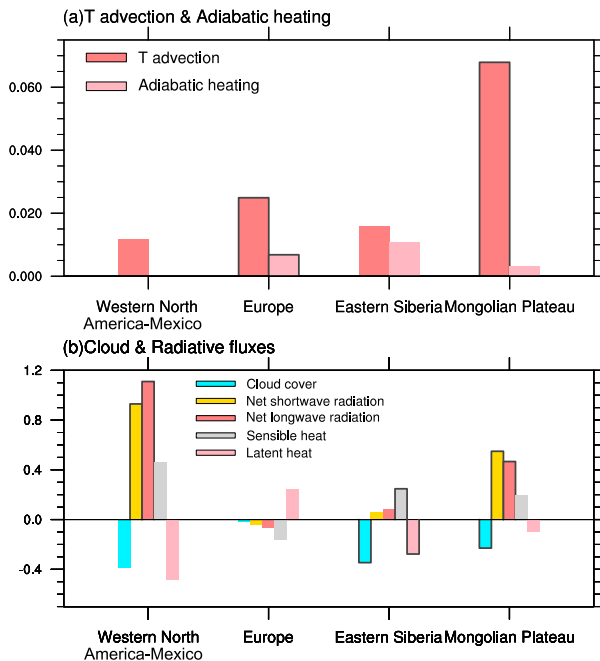


FIG. 6. (a) Temperature advection ( $\text{K day}^{-1}$ ) and adiabatic heating ( $\text{K day}^{-1}$ ) and (b) cloud cover (%), surface net shortwave radiation flux ( $\text{W m}^{-2}$ ; downward is positive), surface net longwave radiation flux ( $\text{W m}^{-2}$ ; upward is positive), latent heat flux ( $\text{W m}^{-2}$ ), and sensible heat flux ( $\text{W m}^{-2}$ ) regressed on the AMO over western North America–Mexico, Europe, eastern Siberia, and the Mongolian Plateau during the time period 1920–2012. The color bars with black borders denote the results that are significant at the 90% confidence level. The temperature budget and adiabatic heating are at 850 hPa for western North America–Mexico and the Mongolian Plateau and 925 hPa for Europe and eastern Siberia.

Berkeley Earth Project (Levi 2013; Rohde et al. 2013a,b). The BEST dataset is a combination of 13 extra sources of station data in addition to the GHCN-daily and contains more than 37 000 individual records. The criteria for the warm days was chosen following Donat et al. (2013). An EHT day refers to a day with a daily maximum temperature exceeding the 90th-percentile calendar day centered on a 5-day window for the base period 1961–90. Using the same thresholds as in section 3, the hotspots characterized by large LF variations in the occurrence and intensity of EHT were identified in this dataset (Fig. 8), which are consistent with those based on GHCNDEX dataset.

When examining the relationship between the decadal to multidecadal variations in temperature over the hotspots and the natural internal variabilities, we noticed the close connection between the four domains (western North America–Mexico, eastern Siberia, Europe, and the Mongolian Plateau) and AMO are still significant in the BEST dataset, which

is consistent with the GISTEMP. Then the NCEP–NCAR reanalysis and ERA-20C datasets were used to verify the physical mechanism linking the AMO and the decadal to multidecadal variability in temperature over these four hotspots based on the 20CR data shown in Figs. 5 and 7 via composite analysis and regression. The results indicate that the influence of the AMO-associated wave train on the variations in temperature over western North America–Mexico, eastern Siberia, Europe, and the Mongolian Plateau is robust because similar results were obtained in all three datasets (figures not shown).

## 7. Summary

The frequency and intensity of EHT in the Northern Hemisphere show remarkable LF variations in the summer during the time period 1951–2017. Five hotspots that are more vulnerable to EHT were identified in both the GHCNDEX and BEST datasets, including western North America–Mexico, eastern Siberia, Europe, central Asia, and the Mongolian Plateau. The LF variations in EHT are consistent with those of the daily mean temperature. Although the LF variations in temperature include both trends and decadal to multidecadal variability, the decadal to multidecadal variations were found to be the major contributors to the LF variance over these hotspots in the last century.

Our main finding is that the large decadal to multidecadal variations in EHT over the four hotspots are the footprints of the AMO (Fig. 9). The AMO contributes to the coherent variation in temperature over western North America–Mexico, eastern Siberia, Europe, and the Mongolian Plateau through a barotropic circumglobal teleconnection. Similar results were obtained in other reanalysis datasets, including the ERA-20C and NCEP–NCAR datasets. The AMO explains 57.6% of the total variance of the decadal to multidecadal variabilities in temperature averaged over these domains. We speculate that the decadal to multidecadal variabilities in temperature over central Asia is modulated by the combined effect of the AMO and SST over northern Indian Ocean.

Our results mainly focused on the influence of natural internal variabilities on the decadal to multidecadal variations in EHT over hotspots. Previous studies have reported that external forcing, including natural and anthropogenic forcing, contributes to the LF variations in global-average temperatures/temperature extremes (Stott et al. 2006; Fischer and Knutti 2015; Schleussner et al. 2017) and regional

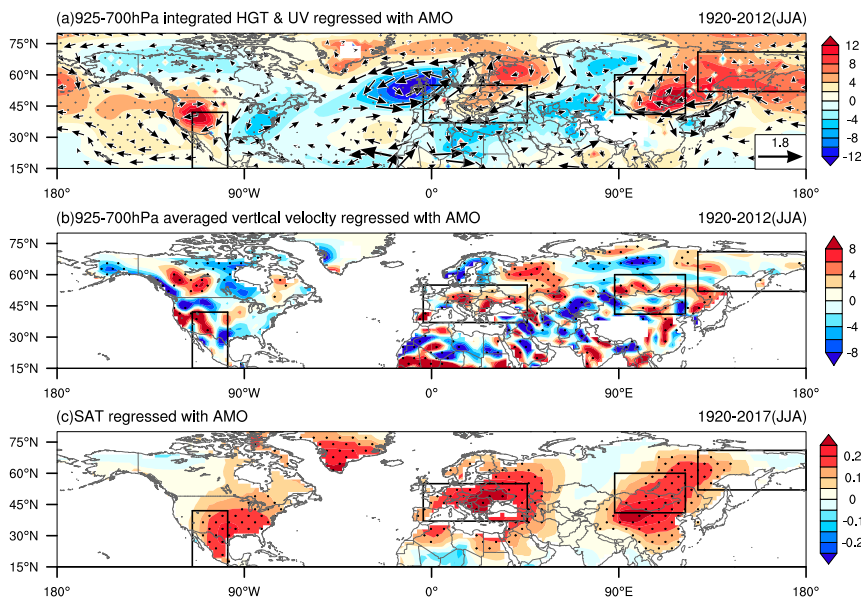


FIG. 7. (a) The 925–700-hPa integrated geopotential height (shading;  $10^2$  gpm) and winds (vectors;  $10^2$  m s $^{-1}$ ), (b) 925–700-hPa integrated vertical velocity ( $10^{-1}$  Pa s $^{-1}$ ), and (c) surface air temperature anomalies ( $^{\circ}$ C) regressed on the AMO. Only the vectors significant at the 95% confidence level are shown in (a). The black dots denote results significant at the 95% confidence level. The black boxes indicate four hotspots, including western North America–Mexico, eastern Siberia, Europe, and Mongolian Plateau.

EHT in eastern China (Sun et al. 2014), Australia (Lewis and Karoly 2013), and Europe (Boer et al. 2000). However, whether and to what extent external forcing could influence the LF variations in EHT over

the hotspots identified in this study requires further analysis using global simulations such as phase 5 of the Coupled Model Intercomparison Project (CMIP5).

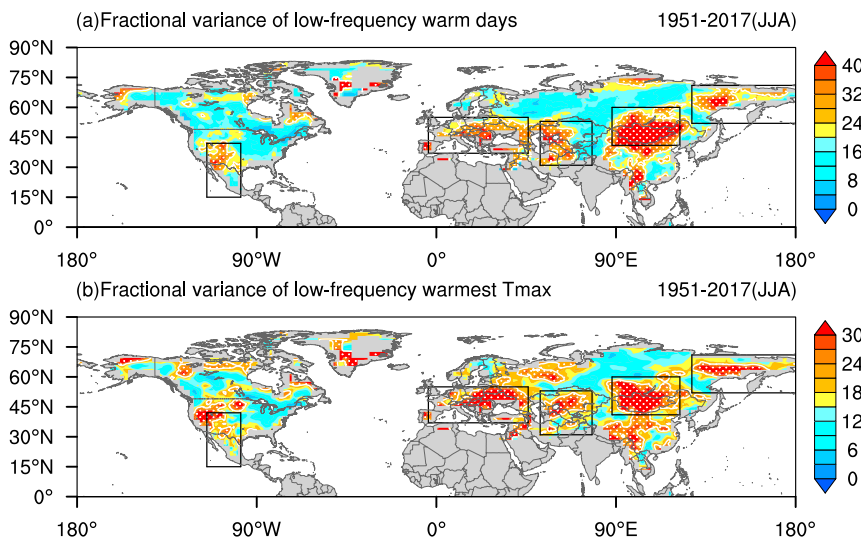


FIG. 8. Spatial distribution of the fractional variance of LF (a) warm days (%) and (b) warmest daily  $T_{\max}$  (%) in JJA during the time period 1951–2017 derived from the BEST dataset. The white dots and lines denote the area with values exceeding top tertile of the grids in the Northern Hemisphere. The black boxes denote the hotspots. Note that the areas with missing values in the GHCNDEX dataset were masked.

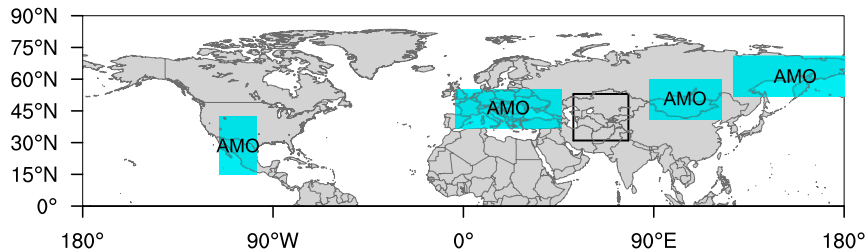


FIG. 9. Schematic diagram of the attribution of AMO to the LF changes in EHT over the hotspots. The five boxes denote the five hotspots. The blue shading indicates that the decadal to multidecadal variations in temperature over these domains are associated with the AMO.

**Acknowledgments.** This study was supported by the funds from the National Key Research and Development Program (Grant 2016YFA0602401), the National Natural Science Foundation of China (Grants 41775071 and 41621061), China Postdoctoral Science Foundation (Grant 2017M620665), the project PE19010 of the Korea Polar Research Institute, and the National Natural Science Foundation of China (Grant 41475043). Dr. Zhangang Han was supported by the National Key Research and Development Program (Grant 2016YFA0602503). The authors acknowledge the constructive suggestions from Dr. Maik Renner from Max-Planck-Institute for Biogeochemistry and Professor Qingxiang Li from Sun Yat-sen University.

#### REFERENCES

- Alexander, L. V., and Coauthors, 2006: Global observed changes in daily climate extremes of temperature and precipitation. *J. Geophys. Res.*, **111**, D05109, <https://doi.org/10.1029/2005JD006290>.
- Boer, G. J., G. Flato, M. C. Reader, and D. Ramsden, 2000: A transient climate change simulation with greenhouse gas and aerosol forcing: Experimental design and comparison with the instrumental record for the twentieth century. *Climate Dyn.*, **16**, 405–425, <https://doi.org/10.1007/s003820050337>.
- Compo, G. P., and Coauthors, 2011: The Twentieth Century Reanalysis Project. *Quart. J. Roy. Meteor. Soc.*, **137**, 1–28, <https://doi.org/10.1002/qj.776>.
- Della-Marta, P. M., M. R. Haylock, J. Luterbacher, and H. Wanner, 2007: Doubled length of western European summer heat waves since 1880. *J. Geophys. Res.*, **112**, D15103, <https://doi.org/10.1029/2007JD008510>.
- Ding, Q., and B. Wang, 2005: Circumglobal teleconnection in the Northern Hemisphere summer. *J. Climate*, **18**, 3483–3505, <https://doi.org/10.1175/JCLI3473.1>.
- Dodla, V. B., G. C. Satyanarayana, and S. Desamsetti, 2017: Analysis and prediction of a catastrophic Indian coastal heat wave of 2015. *Nat. Hazards*, **87**, 395–414, <https://doi.org/10.1007/s11069-017-2769-7>.
- Donat, M. G., L. V. Alexander, H. Yang, I. Durre, R. Vose, and J. Caesar, 2013: Global land-based datasets for monitoring climatic extremes. *Bull. Amer. Meteor. Soc.*, **94**, 997–1006, <https://doi.org/10.1175/BAMS-D-12-00109.1>.
- Dong, B., and A. Dai, 2015: The influence of the interdecadal Pacific oscillation on temperature and precipitation over the globe. *Climate Dyn.*, **45**, 2667–2681, <https://doi.org/10.1007/s00382-015-2500-x>.
- Duchon, C. E., 1979: Lanczos filtering in one and two dimensions. *J. Appl. Meteor.*, **18**, 1016–1022, [https://doi.org/10.1175/1520-0450\(1979\)018<1016:LFIOAT>2.0.CO;2](https://doi.org/10.1175/1520-0450(1979)018<1016:LFIOAT>2.0.CO;2).
- Easterling, D. R., G. A. Meehl, C. Parmesan, S. A. Changnon, T. R. Karl, and L. O. Mearns, 2000: Climate extremes: Observations, modeling, and impacts. *Science*, **289**, 2068–2074, <https://doi.org/10.1126/science.289.5487.2068>.
- Enfield, D. B., A. M. Mestas-Núñez, and P. J. Trimble, 2001: The Atlantic multidecadal oscillation and its relation to rainfall and river flows in the continental U.S. *Geophys. Res. Lett.*, **28**, 2077–2080, <https://doi.org/10.1029/2000GL012745>.
- Eyring, V., S. Bony, G. A. Meehl, C. A. Senior, B. Stevens, R. J. Stouffer, and K. E. Taylor, 2016: Overview of the Coupled Model Intercomparison Project Phase 6 (CMIP6) experimental design and organization. *Geosci. Model Dev.*, **9**, 1937–1958, <https://doi.org/10.5194/gmd-9-1937-2016>.
- Fischer, E. M., and R. Knutti, 2014: Detection of spatially aggregated changes in temperature and precipitation extremes. *Geophys. Res. Lett.*, **41**, 547–554, <https://doi.org/10.1002/2013GL058499>.
- , and —, 2015: Anthropogenic contribution to global occurrence of heavy-precipitation and high-temperature extremes. *Nat. Climate Change*, **5**, 560–564, <https://doi.org/10.1038/nclimate2617>.
- Ghosh, R., W. A. Müller, J. Baehr, and J. Bader, 2017: Impact of observed North Atlantic multidecadal variations to European summer climate: A linear baroclinic response to surface heating. *Climate Dyn.*, **48**, 3547–3563, <https://doi.org/10.1007/s00382-016-3283-4>.
- Grotjahn, R., and Coauthors, 2016: North American extreme temperature events and related large scale meteorological patterns: A review of statistical methods, dynamics, modeling, and trends. *Climate Dyn.*, **46**, 1151–1184, <https://doi.org/10.1007/s00382-015-2638-6>.
- Grumm, R. H., 2011: The central European and Russian heat event of July–August 2010. *Bull. Amer. Meteor. Soc.*, **92**, 1285–1296, <https://doi.org/10.1175/2011BAMS3174.1>.
- Hansen, J., R. Ruedy, M. Sato, and K. Lo, 2010: Global surface temperature change. *Rev. Geophys.*, **48**, RG4004, <https://doi.org/10.1029/2010RG000345>.
- Henley, B. J., J. Gergis, D. J. Karoly, S. Power, J. Kennedy, and C. K. Folland, 2015: A tripole index for the interdecadal Pacific oscillation. *Climate Dyn.*, **45**, 3077–3090, <https://doi.org/10.1007/s00382-015-2525-1>.
- Huang, B., and Coauthors, 2015: Extended Reconstructed Sea Surface Temperature Version 4 (ERSST.v4). Part I: Upgrades and intercomparisons. *J. Climate*, **28**, 911–930, <https://doi.org/10.1175/JCLI-D-14-00006.1>.

- IPCC, 2014: *Climate Change 2014: Synthesis Report*. IPCC, 151 pp.
- Kalnay, E., and Coauthors, 1996: The NCEP/NCAR 40-Year Reanalysis Project. *Bull. Amer. Meteor. Soc.*, **77**, 437–471, [https://doi.org/10.1175/1520-0477\(1996\)077<0437:TNYRP>2.0.CO;2](https://doi.org/10.1175/1520-0477(1996)077<0437:TNYRP>2.0.CO;2).
- Kysely, J., 2009: Recent severe heat waves in central Europe: How to view them in a long-term prospect? *Int. J. Climatol.*, **30**, 89–109, <https://doi.org/10.1002/joc.1874>.
- Lepage, Y., 1971: A combination of Wilcoxon's and Ansari-Bradley's statistics. *Biometrika*, **58**, 213–217, <https://doi.org/10.1093/biomet/58.1.213>.
- Levi, B. G., 2013: Earth's land surface temperature trends: A new approach confirms previous results. *Phys. Today*, **66**, 17–19, <https://doi.org/10.1063/PT.3.1936>.
- Lewis, S. C., and D. J. Karoly, 2013: Anthropogenic contributions to Australia's record summer temperatures of 2013. *Geophys. Res. Lett.*, **40**, 3705–3709, <https://doi.org/10.1002/grl.50673>.
- Liu, W., and Coauthors, 2015: Extended Reconstructed Sea Surface Temperature Version 4 (ERSST.v4): Part II. Parametric and structural uncertainty estimations. *J. Climate*, **28**, 931–951, <https://doi.org/10.1175/JCLI-D-14-00007.1>.
- McCabe, G. J., M. A. Palecki, and J. L. Betancourt, 2004: Pacific and Atlantic Ocean influences on multidecadal drought frequency in the United States. *Proc. Natl. Acad. Sci. USA*, **101**, 4136–4141, <https://doi.org/10.1073/pnas.0306738101>.
- Mondal, A., S. Kundu, and A. Mukhopadhyay, 2012: Rainfall trend analysis by Mann-Kendall test: A case study of north-eastern part of Cuttack District, Orissa. *Int. J. Geol. Earth Environ. Sci.*, **2**, 70–78.
- National Academies of Sciences, Engineering, and Medicine, 2016: *Attribution of Extreme Weather Events in the Context of Climate Change*. National Academies Press, 186 pp.
- Poli, P., and Coauthors, 2016: ERA-20C: An atmospheric reanalysis of the twentieth century. *J. Climate*, **29**, 4083–4097, <https://doi.org/10.1175/JCLI-D-15-0556.1>.
- Qi, L., and Y. Wang, 2012: Changes in the observed trends in extreme temperatures over China around 1990. *J. Climate*, **25**, 5208–5222, <https://doi.org/10.1175/JCLI-D-11-00437.1>.
- Rohde, R., and Coauthors, 2013a: Berkeley Earth temperature averaging process. *Geoinf. Geostat. Overview*, **1**, 1000103, <https://doi.org/10.4172/2327-4581.1000103>.
- , and Coauthors, 2013b: A new estimate of the average Earth surface land temperature spanning 1753 to 2011. *Geoinf. Geostat. Overview*, **1**, 1000101, <https://doi.org/10.4172/2327-4581.1000101>.
- Rohini, P., M. Rajeevan, and A. K. Srivastava, 2016: On the variability and increasing trends of heat waves over India. *Sci. Rep.*, **6**, 26153, <https://doi.org/10.1038/srep26153>.
- Ruprich-Robert, Y., T. Delworth, R. Msadek, F. Castruccio, S. Yeager, and G. Danabasoglu, 2018: Impacts of the Atlantic multidecadal variability on North American summer climate and heat waves. *J. Climate*, **31**, 3679–3700, <https://doi.org/10.1175/JCLI-D-17-0270.1>.
- Schleussner, C.-F., P. Pfleiderer, and E. M. Fischer, 2017: In the observational record half a degree matters. *Nat. Climate Change*, **7**, 460–462, <https://doi.org/10.1038/nclimate3320>; Corrigendum, **8**, 257, <https://doi.org/10.1038/s41558-017-0055-z>.
- Si, D., and Y. Ding, 2016: Oceanic forcings of the interdecadal variability in East Asian summer rainfall. *J. Climate*, **29**, 7633–7649, <https://doi.org/10.1175/JCLI-D-15-0792.1>.
- Stott, P. A., D. A. Stone, and M. R. Allen, 2004: Human contribution to the European heatwave of 2003. *Nature*, **432**, 610–614, <https://doi.org/10.1038/nature03089>; Corrigendum, **436**, 1200, <https://doi.org/10.1038/nature04099>.
- , J. F. B. Mitchell, M. R. Allen, T. L. Delworth, J. M. Gregory, G. A. Meehl, and B. D. Santer, 2006: Observational constraints on past attributable warming and predictions of future global warming. *J. Climate*, **19**, 3055–3069, <https://doi.org/10.1175/JCLI3802.1>.
- Sun, C., J. Li, and S. Zhao, 2015: Remote influence of Atlantic multidecadal variability on Siberian warm season precipitation. *Sci. Rep.*, **5**, 16853, <https://doi.org/10.1038/srep16853>.
- , F. Kucharski, J. Li, F.-F. Jin, I.-S. Kang, and R. Ding, 2017: Western tropical Pacific multidecadal variability forced by the Atlantic multidecadal oscillation. *Nat. Commun.*, **8**, 15998, <https://doi.org/10.1038/ncomms15998>.
- Sun, Y., X. Zhang, F. W. Zwiers, L. Song, H. Wan, T. Hu, H. Yin, and G. Ren, 2014: Rapid increase in the risk of extreme summer heat in eastern China. *Nat. Climate Change*, **4**, 1082–1085, <https://doi.org/10.1038/nclimate2410>.
- Sutton, R. T., and D. L. R. Hodson, 2005: Atlantic Ocean forcing of North American and European summer climate. *Science*, **309**, 115–118, <https://doi.org/10.1126/science.1109496>.
- Wang, J., Z. Yan, X.-W. Quan, and J. Feng, 2017: Urban warming in the 2013 summer heat wave in eastern China. *Climate Dyn.*, **48**, 3015–3033, <https://doi.org/10.1007/s00382-016-3248-7>.
- Wang, L., Z.-J. Yao, L.-G. Jiang, R. Wang, S.-S. Wu, and Z.-F. Liu, 2016: Changes in climate extremes and catastrophic events in the Mongolian Plateau from 1951 to 2012. *J. Appl. Meteor. Climatol.*, **55**, 1169–1182, <https://doi.org/10.1175/JAMC-D-14-0282.1>.
- Watanabe, T., and K. Yamazaki, 2014a: The upper-level circulation anomaly over central Asia and its relationship to the Asian monsoon and mid-latitude wave train in early summer. *Climate Dyn.*, **42**, 2477–2489, <https://doi.org/10.1007/s00382-013-1888-4>.
- , and —, 2014b: Decadal-scale variation of South Asian summer monsoon onset and its relationship with the Pacific decadal oscillation. *J. Climate*, **27**, 5163–5173, <https://doi.org/10.1175/JCLI-D-13-00541.1>.
- Wibig, J., 2018: Heat waves in Poland in the period 1951–2015: Trends, patterns and driving factors. *Meteor. Hydrol. Water Manage.*, **6**, 37–45, <https://doi.org/10.26491/mhwm/78420>.
- Wu, B., T. Zhou, and T. Li, 2016: Impacts of the Pacific–Japan and circumglobal teleconnection patterns on the interdecadal variability of the East Asian summer monsoon. *J. Climate*, **29**, 3253–3271, <https://doi.org/10.1175/JCLI-D-15-0105.1>.
- Yanai, M., S. Esbensen, and J.-H. Chu, 1973: Determination of bulk properties of tropical cloud clusters from large-scale heat and moisture budgets. *J. Atmos. Sci.*, **30**, 611–627, [https://doi.org/10.1175/1520-0469\(1973\)030<0611:DOBPOT>2.0.CO;2](https://doi.org/10.1175/1520-0469(1973)030<0611:DOBPOT>2.0.CO;2).
- Zhou, Y., and Z. Wu, 2016: Possible impacts of mega-El Niño/Southern Oscillation and Atlantic multidecadal oscillation on Eurasian heatwave frequency variability. *Quart. J. Roy. Meteor. Soc.*, **142**, 1647–1661, <https://doi.org/10.1002/qj.2759>.
- Zwiers, F. W., and H. von Storch, 1995: Taking serial correlation into account in tests of the mean. *J. Climate*, **8**, 336–351, [https://doi.org/10.1175/1520-0442\(1995\)008<0336:TSCIAI>2.0.CO;2](https://doi.org/10.1175/1520-0442(1995)008<0336:TSCIAI>2.0.CO;2).